Giant enhancement of solid solubility in monolayer alloys by selective orbital coupling

Shiqiao Du,[1,2] Jianfeng Wang,[2] Lei Kang,[2] Bing Huang,[2,*] and Wenhui Duan[1]
[1]*Department of Physics and State Key Laboratory of Low-Dimensional Quantum Physics, Tsinghua University, Beijing 100084, China*
[2]*Beijing Computational Science Research Center, Beijing 100193, China*

(Received 23 January 2019; revised manuscript received 15 January 2020; accepted 21 January 2020; published 5 February 2020)

Solid solubility (SS) is one of the most important features of alloys, which is difficult to be largely tuned in the entire alloy concentrations by external approaches, e.g., the case for monolayer BNC [$(BN)_{1-x}(C_2)_x$] alloys. Here a novel mechanism of selective orbital coupling between wrong-bond states and surface states mediated by the specific substrate has been proposed to stabilize the wrong bonds and in turn significantly enhance the SS of $(BN)_{1-x}(C_2)_x$. Surprisingly, we demonstrate that five ordered alloys can spontaneously be formed when $(BN)_{1-x}(C_2)_x$ is grown on hcp-phase Cr. These ordered alloys can exhibit largely tunable quasiparticle band gaps (1.45–3.91 eV) and exciton binding energies (0.5–1.6 eV) in their free-standing forms. Importantly, the disordered $(BN)_{1-x}(C_2)_x$ can be achieved on Cr substrate with a hugely reduced miscibility temperature from 5600 to 1200 K. These disordered alloys exhibit continuously tunable band gaps from 0 to 6 eV in their free-standing forms. Our discovery could potentially resolve the long-standing SS problem of BNC alloys and significantly extend their optoelectronic applications from infrared to deep ultraviolet.

DOI: 10.1103/PhysRevB.101.054201

I. INTRODUCTION

Solid solubility (SS) is one of the most critical features for all the alloys, which fundamentally determines their overall physical properties, including electronic [1–3], magnetic [4,5], plasmonic [6,7], defect [8–10], and catalytic properties [11,12], etc. In the past decades, several approaches have been developed to enhance the SS of alloys via the development of various specific growth conditions [6–8,11,13]. In particular, the SS of semiconducting alloys not only depends on their intrinsic structural properties, but also strongly depends on the electronic structures of the host materials [1–5,8–10,14]. The existence of strong phase inhomogeneity, caused by the poor SS, has been a big issue to restrict many semiconducting alloys in their practical applications.

Nitrides have great potentials for solid-state lighting (SSL) [15]. $In_{1-x}Ga_xN$ alloys have appeared to be one of the most important monolithic alloys for white light-emitting diodes (LEDs). Unfortunately, the poor SS around $x = 0.5$ in $In_{1-x}Ga_xN$, induced by the large lattice mismatch (>10%) between InN and GaN, have strongly restricted their efficiency for white SSL [15,16]. Since two-dimensional (2D) boron nitride (BN) was discovered as a promising material for deep-UV SSL [17,18], tremendous efforts have been developed to alloying graphene into BN forming BNC solid solutions in order to realize a tunable band gap (E_g) in the entire visible spectrums, so that they might replace $In_{1-x}Ga_xN$ for white SSL [19–31]. However, although the lattice mismatch between BN and graphene is much smaller (<2%) than that of $In_{1-x}Ga_xN$, it is widely found that the SS of BNC is even much poorer than that of $In_{1-x}Ga_xN$ [19–31], mostly due to the imbalanced valence electrons of alloyed elements.

In the experiments, ammonia borane (BNH_6) molecules are widely adopted as precursors to epitaxially grow BN or BNC alloys [19,32,33], which means that the amount of B and N atoms are mostly equal in the BNC, i.e., forming $(BN)_{1-x}(C_2)_x$ alloys. Although extensive experimental studies have been done on the SS issue of $(BN)_{1-x}(C_2)_x$ in the past decade [19–27], an effective approach to realize the $(BN)_{1-x}(C_2)_x$ solid solutions in the entire x is still unachievable. Meanwhile, in the previous theoretical studies [28–31], an effective mechanism for realizing ordered or disordered $(BN)_{1-x}(C_2)_x$ solid solutions is unknown. Therefore, $(BN)_{1-x}(C_2)_x$ alloys, dominated by the large-scale BN and C domains, mostly behave as very poor electronic properties instead of widely tunable E_g in all the experiments [19–21,23–27].

It is expected that the reduction of structural dimensionality from three dimensions (3D) to 2D could bring new opportunities to modulate the SS of an alloy system. In this article we have developed an effective concept to overcome the phase inhomogeneity in $(BN)_{1-x}(C_2)_x$. Importantly, a novel mechanism of symmetry-allowed selective orbital coupling between high energy wrong-bond states and specific substrate-mediated surface states has been proposed to stabilize the wrong-bond states and in turn significantly enhances the SS of $(BN)_{1-x}(C_2)_x$. Surprisingly, we demonstrate that five ordered $(BN)_{1-x}(C_2)_x$ alloys can be spontaneously formed at different x when $(BN)_{1-x}(C_2)_x$ is grown on hcp-phase Cr(0001). These ground states have a widely tunable direct quasiparticle E_g from 1.45 to 3.91 eV in their free-standing forms. Meanwhile, the optical transitions around the band edges in these ordered alloys are extremely strong, accompanied by largely tunable exciton binding energies (E_b) from 0.5 to 1.6 eV at different x. Remarkably, it is found that the miscibility temperature (T_c) of $(BN)_{1-x}(C_2)_x$ grown on Cr(0001) can be dramatically reduced from ~5600 to ~1200 K. The disordered $(BN)_{1-x}(C_2)_x$

*Bing.Huang@csrc.ac.cn

alloys, exhibiting a continuously tunable E_g from 0 to 6 eV in their free-standing forms, could be the ideal monolithic alloys that can cover the entire energy regions from infrared to deep ultraviolet.

II. RESULTS

The $(BN)_{1-x}(C_2)_x$ system can be effectively considered as a quasibinary system [29,34], so that the cluster expansion (CE) theory based on first-principles calculations can be applied to calculate the formation energies (E_f) of a large number of $(BN)_{1-x}(C_2)_x$ alloys [14,35]. The basic idea of CE is to expand the energies of a $(BN)_{1-x}(C_2)_x$ configuration into energy contributions of cluster figures (single atoms, pairs, triples, etc.) based on a generalized Ising Hamiltonian:

$$E(\sigma) = J_0 + \sum_i J_i + \sum_{i<j} J_{ij}\hat{S}_i(\sigma)\hat{S}_j(\sigma) + \sum_{i<j<k} J_{ijk}\hat{S}_i(\sigma)\hat{S}_j(\sigma)\hat{S}_k(\sigma) + \cdots . \quad (1)$$

The indexes i, j, and k run over all the alloy sites, and $S_m(\sigma)$ is set to $+1$ (-1) when it is occupied by BN (C_2) dimer. It is noted that the first two terms on the right-band side of Eq. (1) define the linear dependence of the energy of a $(BN)_{1-x}(C_2)_x$ configuration as a function of x, while the third and fourth terms contain all pair and three-body interactions, etc. Every cluster figure is associated with an effective cluster interaction (ECI) J_α, which indicates the energy contribution of a specific cluster figure to the total energy. Ideally, the CE can represent any $(BN)_{1-x}(C_2)_x$ alloy energy $E(\sigma)$ by the appropriate selection of J_α, which can be fitted from first-principles total energy calculations based on a sufficient number of alloy configurations [14]. The cross-validation score is set to 0.05 eV and we have further confirmed the convergence of our CE fitting by adding more alloy configurations in the test calculations. To calculate the binary phase diagram of $(BN)_{1-x}(C_2)_x$, Monte Carlo (MC) simulations, which sample a semi-grand-canonical ensemble, are carried out in which the energetics of $(BN)_{1-x}(C_2)_x$ are specified by the CE Hamiltonian [36].

Overall, we find that the strong phase separation in $(BN)_{1-x}(C_2)_x$ is mostly due to the high-energy cost of forming B-C and N-C wrong bonds. In BN (graphene), the formation of B-N (C-C) bonds meets the octet rule that can make the π_{BN} (π_{CC}) bonding states fully occupied and antibonding π^*_{BN} (π^*_{CC}) states fully unoccupied, as shown in the left (right) panel of Fig. 1. Meanwhile, the large π_{BN}-π^*_{BN} (π_{CC}-π^*_{CC}) separation due to the ionic charge transfer (covalent hybridization) during the formation of B-N (C-C) bonds can significantly push the π_{BN} (π_{CC}) states down to a low energy position. As shown in Fig. 1, π_{BN} and π_{CC} finally reach a similar energy position in terms of our DFT calculations.

During the formation of $(BN)_{1-x}(C_2)_x$, the unavoidable B-C and N-C wrong bonds do not meet the octet rule. As shown in Fig. 1 (middle panel), compared to π_{BN}/π_{CC}, π_{BC} is pushed down to a higher energy position because the strength of orbital coupling in a C-B bond is weaker than that of B-N/C-C bonds, as indicated by their calculated bond

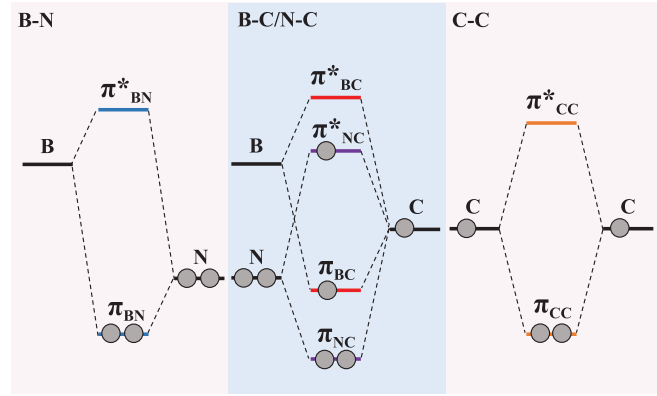

FIG. 1. Schematic representation of the formation of bonding π and antibonding π^* states in B-N (left), B-C/N-C (middle), and C-C (right) bonds, respectively.

lengths ($d_{C\text{-}B} = 1.52$ Å, $d_{B\text{-}N} = 1.4$ Å, and $d_{C\text{-}C} = 1.42$ Å). Meanwhile, π_{BC} can only be partially occupied based on the electron counting. On the other hand, although π_{NC} can be pushed down to a lower energy position than that of π_{BN}/π_{CC}, due to the stronger N-C orbital coupling strength ($d_{N\text{-}C} = 1.38$ Å), the high-energy π^*_{NC} is unavoidable to be partially occupied based on the electron counting. In practice, the charge transfer from π^*_{NC} to π_{BC} may occur to make the π^*_{NC} (π_{BC}) orbitals fully empty (occupied), in order to lower the total energy of the system. Therefore, it turns out that the high energy position of (occupied) π_{BC} could be the most critical factor that make the wrong bonds in $(BN)_{1-x}(C_2)_x$ unstable. Consequently, large BN and C domains are always forming in a $(BN)_{1-x}(C_2)_x$, i.e., the less number of wrong bonds, the lower total energy the $(BN)_{1-x}(C_2)_x$.

The key to enhance SS of $(BN)_{1-x}(C_2)_x$ is to stabilize the B-C and N-C wrong bonds, i.e., the π_{BC} level must be pushed down to a comparable or even lower energy position than that of π_{BN}/π_{CC}. In a conventional 3D alloy, it is extremely difficult to modulate the orbital levels of wrong bonds hidden in the bulk via external approaches. However, it is expected that the reduction of alloy dimensionality from 3D to 2D could bring new opportunities to modulate its SS, as the surface wrong-bond orbitals are touchable and could be further modulated by its surrounding environments. In practice, since $(BN)_{1-x}(C_2)_x$ alloys are usually grown on a variety of transition-metals (TMs), e.g., fcc-phase Cu and Ni [19–24,37], by CVD methods, the external orbital coupling could occur at the surfaces of underneath TMs. Unfortunately, an effective concept on substrate-enhanced SS in $(BN)_{1-x}(C_2)_x$ is still lacking, which is the main purpose of our study.

First, we have systematically calculated the E_f of free-standing $(BN)_{1-x}(C_2)_x$, which is defined as

$$E_f = E[(BN)_{1-x}(C_2)_x] - (1-x)\mu_{BN} - x\mu_{C_2}, \quad (2)$$

where μ_{BN} (μ_{C_2}) is the energy of the BN (C_2) unit cell. For free-standing $(BN)_{1-x}(C_2)_x$, the E_f of selected 29 $(BN)_{1-x}(C_2)_x$ structures are calculated using DFT methods, as shown in Fig. 2(a). Second, these J_α values defining CE are fitting to these 29 DFT energies, and the CE includes 16 J_α up to four-point clusters, as shown in Fig. 2(c). Apparently,

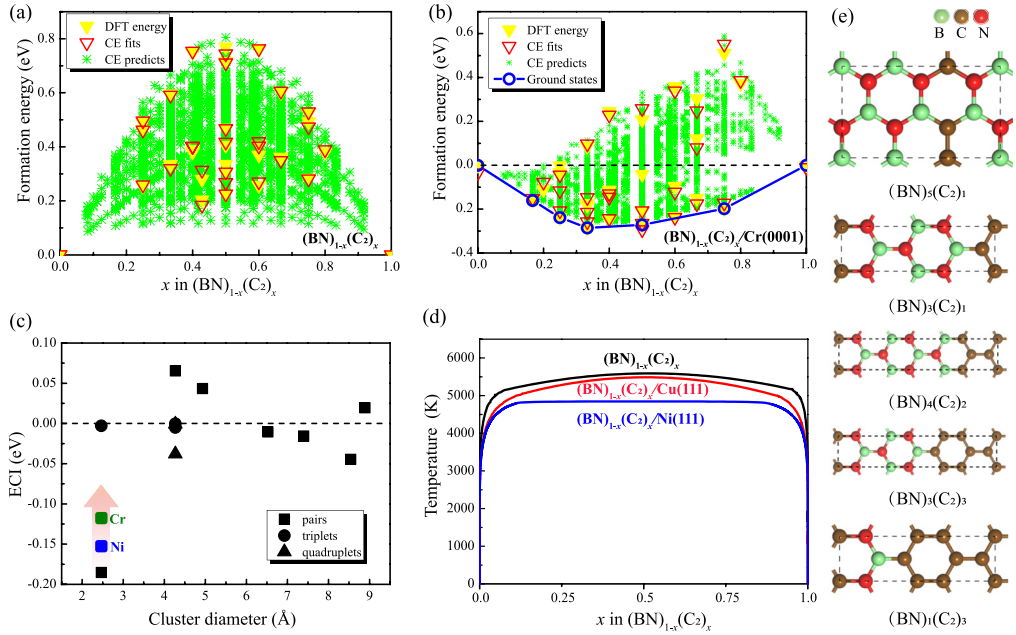

FIG. 2. Calculated formation energies (E_f) of $(BN)_{1-x}(C_2)_x$ (with respect to graphene and BN) along with the corresponding CE fits as a function of x in (a) free-standing $(BN)_{1-x}(C_2)_x$ and (b) $(BN)_{1-x}(C_2)_x$/Cr(0001). The E_f of 2280 and 3020 symmetry-inequivalent $(BN)_{1-x}(C_2)_x$ structures up to 24 atoms/cell calculated from CE are also plotted in (a) and (b), respectively. (c) Effective cluster interactions J_α as a function of cluster diameter for free-standing $(BN)_{1-x}(C_2)_x$, fitted with CE. The dominated $J_{\alpha\text{-NN}}$ for $(BN)_{1-x}(C_2)_x$/Ni(111) and $(BN)_{1-x}(C_2)_x$/Cr(0001) are also plotted here for comparison. (d) MC-calculated phase diagrams of $(BN)_{1-x}(C_2)_x$ with and without Ni or Cu substrates. (e) Structures of five ordered intermediate $(BN)_{1-x}(C_2)_x$ ground states in (b), in which the unit cells are enclosed by the dashed lines. The green, brown, and red balls represent boron, carbon, and nitrogen atoms, respectively.

J_α are dominated by negative values and the largest negative J_α is contributed by the nearest-neighboring ($J_{\alpha\text{-NN}}$) BN-BN (or C_2-C_2) pair attractive interactions, i.e., BN (C_2) always prefers to bond with BN (C_2) forming large-scale BN (C) domains. Finally, the constructed CE are then used to calculate the E_f of all the enumerated symmetry-inequivalent alloy structures up to 24 atoms/cell. As shown in Fig. 2(a). There is no intermediate ground state for $0 < x < 1$, i.e., the ground state of a $(BN)_{1-x}(C_2)_x$ will separate into BN and graphene, and the E_f of metastable $(BN)_{1-x}(C_2)_x$ distribute in a wide range of $0.1 < E_f < 0.8$ eV, consistent with the dominated negative J_α values [14]. The phase diagram of free-standing $(BN)_{1-x}(C_2)_x$ is calculated by CE-based MC simulations, as shown in Fig. 2(d). The miscibility temperature $T_c \sim 5600$ K in $(BN)_{1-x}(C_2)_x$, which is too high to be achieved (even higher than the melting point of graphene).

It is curious to further understand the substrate effects on the SS of $(BN)_{1-x}(C_2)_x$. Here the Cu(111) and Ni(111) are selected as representatives not only because they are widely adopted in the current experiments, but also because they are convenient for affordable large-scale alloy calculations with small lattice mismatch (<2%) (See Table 1 in the Supplemental Material [38]). For the $(BN)_{1-x}(C_2)_x$/TM system, the ground states of hosts, i.e., BN/TM and C/TM, are first determined by extensive calculations and then the alloy properties of $(BN)_{1-x}(C_2)_x$/TM are calculated following a similar DFT-CE-MC process as that for free-standing $(BN)_{1-x}(C_2)_x$. Overall, the crystal field induced by the D_{3d} symmetry of Cu(111) [or Ni(111)] gives rise to d-orbital filling of surface atoms into two double-degenerate states [e_g' ($d_{xy} + d_{x^2}$) and e_g ($d_{xz} + d_{yz}$)] and single state a_{1g} (d_{z^2}). The wave functions of e_g', e_g, and a_{1g} orbitals are delocalized, and a_{1g} is the only symmetry-allowed d orbital having strong nonzero overlap with the π_{BC} level.

For Cu(111), its surface d orbitals are fully occupied (closed shell) and ~5 eV below the Fermi level (see Fig. S1 in the Supplemental Material [38]), which cannot couple with π_{BC}. As a result, the calculated (average) interfacial binding energy (E_{int}) between a (metastable) $(BN)_{1-x}(C_2)_x$ and Cu(111) surface is ~62 meV/atom, belonging to weak interactions. No intermediate ground state is found for $0 < x < 1$ in $(BN)_{1-x}(C_2)_x$/Cu(111) (see Figs. S2 and S3 in the Supplemental Material [38]). As shown in Fig. 2(d), the calculated $T_c \sim 5300$ K is slightly lower than that of free-standing $(BN)_{1-x}(C_2)_x$, explaining well the experimental observations of inhomogeneous $(BN)_{1-x}(C_2)_x$ on Cu(111) at a growth temperature of ~1000 K [19–21].

For Ni(111), its surface d_{z^2} orbitals are located around the Fermi level, but they are close to be fully (~90%) occupied (see Fig. S1 in the Supplemental Material [38]). Therefore, no sufficiently empty d_{z^2} orbitals are available to effectively couple with π_{BC} lowering its wrong-bond energies. The calculated (average) E_{int} between a (metastable) $(BN)_{1-x}(C_2)_x$ and Ni(111) surface is ~115 meV/atom. Although no intermediate ground state is found between $0 < x < 1$ (see Figs. S4 and S5 in the Supplemental Material [38]), the weak d_{z^2}-π_{BC} hybridization in $(BN)_{1-x}(C_2)_x$/Ni(111) can still reduce the strength of $J_{\alpha\text{-NN}}$ [Fig. 2(c)] and in turn slightly reduce its T_c [Fig. 2(d)]. Indeed, the calculated $T_c \sim 4850$ K for $(BN)_{1-x}(C_2)_x$/Ni(111), which is ~450 K lower than that of $(BN)_{1-x}(C_2)_x$/Cu(111) but still impossible to be achieved [21,37].

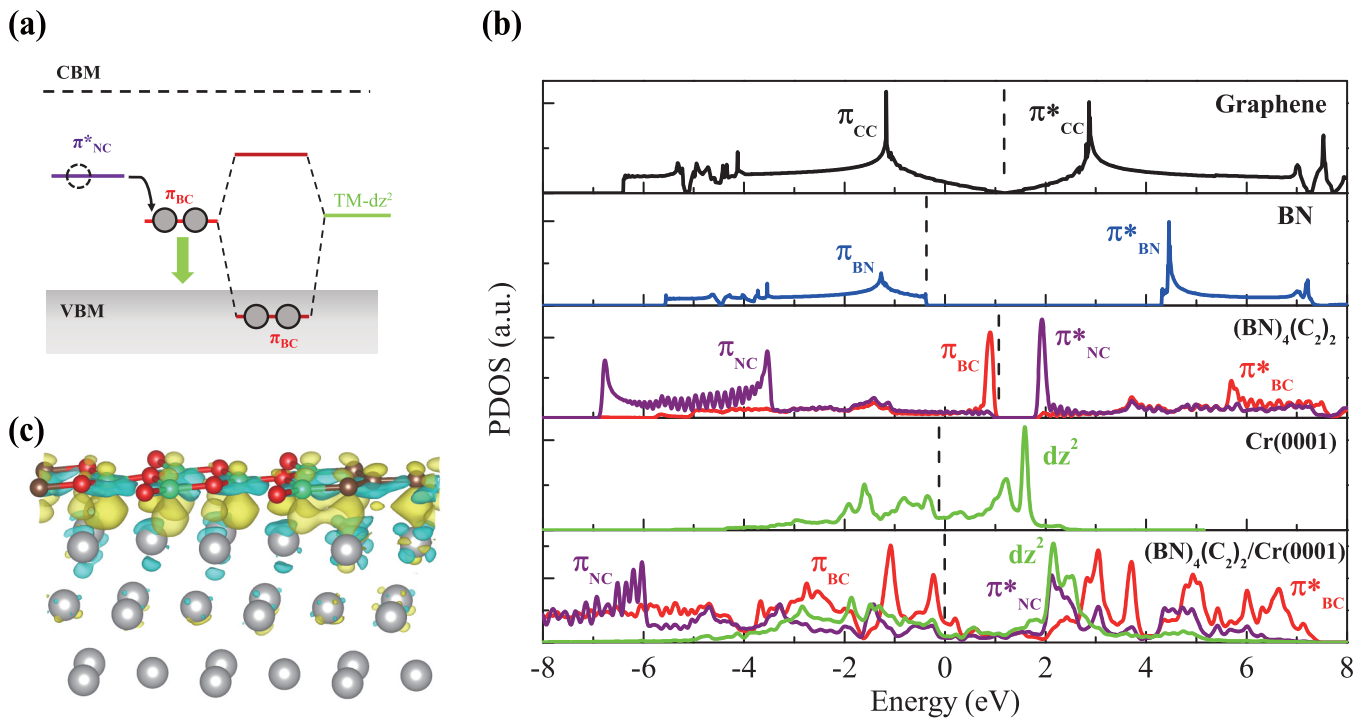

FIG. 3. (a) Schematic diagram of the mechanism of selective orbital coupling between π_{BC} of a $(BN)_{1-x}(C_2)_x$ and d_{z^2} of an ideal TM substrate. (b) Projected density of states (PDOS) of graphene, BN, $(BN)_4(C_2)_2$, Cr(0001), and $(BN)_4(C_2)_2$/Cr(0001). It is noted that only the d_{z^2} orbitals contributed by the Cr surface atoms are plotted here. All PDOS, calculated using the PBE functional, are aligned with the vacuum level and Fermi level positions are marked as dashed lines. (c) Calculated charge density difference for the ground-state $(BN)_4(C_2)_2$ on Cr(0001). The yellow (cyan) areas show where the electron density has been enriched (depleted). The green, brown, red, and silver represent B, C, N, and Cr, respectively.

Obviously, Cu and Ni, widely adopted in the experiments, are not ideal substrates for growing homogenous $(BN)_{1-x}(C_2)_x$. There are two important criteria for an ideal TM substrate: (1) the surface states hosted by the TM should have sufficient empty d_{z^2} orbitals and (2) the energy position of empty d_{z^2} orbitals should match well with that of π_{BC}. In this situation, a key mechanism of selective d_{z^2}-π_{BC} orbital hybridization can occur: as demonstrated in Fig. 3(a), the surface empty d_{z^2} orbitals can have a much stronger covalent hybridization with π_{BC} than π_{BN}/π_{CC}; after charge transfer from π^*_{NC} to π_{BC}, the fully occupied π_{BC} could be significantly pushed down. This mechanism can effectively stabilize the wrong-bond states in $(BN)_{1-x}(C_2)_x$ and therefore greatly enhance its SS.

Based on the extensive calculations, we successfully discover that the hcp-phase Cr, a metastable Cr phase existing in the experiments [39,40], is such an ideal substrate example for realizing this mechanism. The lattice mismatch between Cr(0001) and $(BN)_{1-x}(C_2)_x$ is also small (<2%) (see Table S1 in the Supplemental Material [38]). As shown in Fig. 2(c), the calculated strength of $J_{\alpha\text{-NN}}$ is largely reduced in $(BN)_{1-x}(C_2)_x$/Cr(0001) compared to that of free-standing $(BN)_{1-x}(C_2)_x$, which can effectively balance the repulsive and attractive cluster interactions and therefore result in well-ordered ground states [14]. Interestingly, five intermediate ordered lowest energy states with specific stoichiometries, i.e., $(BN)_5(C_2)_1$, $(BN)_3(C_2)_1$, $(BN)_4(C_2)_2$, $(BN)_3(C_2)_3$, and $(BN)_1(C_2)_3$, are spontaneously formed in the $(BN)_{1-x}(C_2)_x$/Cr(0001) systems, as shown in Figs. 2(b) and 2(e) (see Figs. S6 and S7 in the Supplemental Material [38]). To further confirm the reliability of our quasi-binary-CE-based structural search, we have considered a more general situation of BNC ternary alloys on Cr(0001) based on the ternary-CE-based structural search approaches [41]. As shown in Fig. S8 in the Supplemental Material [38], the additional calculations further confirm that these lowest energy states shown in Fig. 2(e) are reliable.

For these lowest energy states on Cr(0001), the calculated average E_f is ~210 meV/atom. For Cr(0001), its delocalized surface d_{z^2} orbitals, located around Fermi level, are half (~50%) occupied (see Fig. S1 in the Supplemental Material [38]), which means that a sufficient amount of empty d_{z^2} orbitals are available for d_{z^2}-π_{BC} coupling. Taking the lowest energy state $(BN)_4(C_2)_2$/Cr(0001) as a typical example, the positions of Cr-d_{z^2} empty states match well with that of π_{BC} in energy, as shown in Fig. 3(b). Therefore, the strong d_{z^2}-π_{BC} coupling can significantly broaden, split, and then push π_{BC} down to a much lower energy positions (even lower than that of π_{BN}/π_{CC} for a large percentage of π_{BC} states) and resonant inside the valence band. Meanwhile, it is found that the d_{z^2} -π^*_{NC} orbital coupling can also push the empty π^*_{NC} states down below the VBM to be partially occupied and therefore gain energy, as shown in Fig. 3(b). However, the orbital coupling strength between d_{z^2}-π_{BC} is significantly stronger than that between d_{z^2} -π^*_{NC}. After selective orbital coupling of d_{z^2}-π_{BC} and d_{z^2} -π^*_{NC}, the B-C/N-C wrong-bond states can be successfully stabilized in $(BN)_{1-x}(C_2)_x$/Cr(0001). We have

further plotted the charge density difference before and after the $(BN)_4(C_2)_2$ grows on Cr(0001), as shown in Fig. 3(c). Interestingly, the largest charge transfer occurs around the region between the B-C wrong bonds and Cr(0001), which further confirms that the orbital hybridization of d_{z^2}-π_{BC} is stronger than that of d_{z^2} -π^*_{NC}.

The large bond-length differences between B-C/N-C and B-N/C-C bonds in $(BN)_{1-x}(C_2)_x$ can induce local imbalanced strain fields, which is configuration dependent and can cost energy. The competition between energy gain (from orbital coupling) and energy cost (from the local strains) will effectively determine the structural characteristics (e.g., ultranarrow BN-C nanoribbon superlattice structures [Fig. 2(e)]) as well as the amount of wrong bonds in the $(BN)_{1-x}(C_2)_x$ ground states. To confirm our intuition, taking $(BN)_3(C_2)_3$ as a typical example, we have constructed a sufficient number of $(BN)_3(C_2)_3$ configurations that have much more wrong bonds than the lowest energy state structure shown in Fig. 2(e). Generally, we find that all of these (metastable) structures have larger strain energies and higher E_f than that of the ground-state one (see Fig. S9 and Table S4 in the Supplemental Material [38]). Therefore, the configurations with a larger number of wrong bonds could have larger structural strain fields and higher E_f compared to that of lowest energy state configurations.

We have systemically checked the dynamical and thermal stability of (free-standing) ordered $(BN)_{1-x}(C_2)_x$ monolayers after exfoliation using first-principles phonon spectrum and molecular dynamical (MD) calculations, respectively. As shown in Fig. S10 in the Supplemental Material [38], no imaginary frequency is found in the phonon spectra of these five ordered $(BN)_{1-x}(C_2)_x$, which means that they are dynamically stable. To confirm the thermal stability of the ground states, the large supercells of >120 atoms are constructed for these five ordered alloys. The first-principles MD simulations are performed with a Nose-Hoover thermostat at 1500 K. Figure S11 in the Supplemental Material [38] shows the fluctuation of total energies of these structures as a function of simulation times. After 25 ps, no structural destruction is found in these structures, except that the thermal fluctuations can induce rippled structures (generally exist in all the free-standing 2D materials at finite temperature). Our calculations strongly indicate that the sp^2-B-N-C bonds in $(BN)_{1-x}(C_2)_x$ monolayers are stable even under high temperature of (at least) 1500 K.

It is interesting to understand the intrinsic optoelectronic properties of discovered ordered $(BN)_{1-x}(C_2)_x$ ground states in their free-standing forms. The quasiparticle band structures of these five ordered $(BN)_{1-x}(C_2)_x$ alloys are calculated based on *GW* calculations (at the G_0W_0 level). The excitonic effects of these five ordered $(BN)_{1-x}(C_2)_x$ lowest energy states are then considered by solving the Bethe-Salpeter equation (BSE) based on their calculated quasiparticle band structures. As a benchmark, the *GW* band structure and optical spectrum of monolayer BN are calculated (see Fig. S12 in the Supplemental Material [38]), which is in good agreement with the previous calculations [42,43]. We have also calculated the band structures of five ordered states using PBE functional and HSE06 functional (see Fig. S13 in the Supplemental Material [38]). The shapes of these band structures are similar, except that the *GW* band gaps are ∼0.7 eV larger than that of HSE06 band gap.

As shown in Fig. 4(a), all these five lowest energy states have promising direct gaps ranging from 1.45 to 3.91 eV. The conduction and valence band edges of these band structures are contributed by π^*_{NC} and π_{BC} states, respectively, which can induce relatively flat band dispersions in some structures, e.g., $(BN)_3(C_2)_1$ and $(BN)_4(C_2)_2$. It is expected that these flat bands around the band edges can result in high electron-hole pair intensities during either the optical absorption or emission [44].

As a typical example, Fig. 4(b) shows the calculated absorption spectra of $(BN)_3(C_2)_1$ with electron-hole interaction (*GW*-BSE) and without electron-hole interaction (*GW*-RPA). The optical spectra of other four ordered $(BN)_{1-x}(C_2)_x$ alloys can be found in Fig. S14 in the Supplemental Material [38]. Indeed, the calculated absorption spectra confirm that the optical dipole transitions between π^*_{NC} and π_{BC} at these band edges are not only allowed but also have similar intensities to that of BN. As shown in Fig. 4(b), the *GW*-BSE-calculated optical spectrum of $(BN)_3(C_2)_1$ features a strong absorption peak (marked as A) at ∼1.84 eV, which is contributed by the band-edge optical transitions occurring at these k points associated with flat bands, as shown in inset of Fig. 4(b).

As shown in Fig. 4(c), the *GW* band gaps ($E_{g\text{-}GW}$) of these ordered $(BN)_{1-x}(C_2)_x$ decrease as x increases. Overall, the E_b of these five ordered $(BN)_{1-x}(C_2)_x$ decreases as their $E_{g\text{-}GW}$ decreases, which can been significantly tuned in a very large range of ∼1 eV by adjusting x. It notes that the E_b is determined by the energy difference of the first absorption peak at the absorption edges, e.g., A in Fig. 4(b), between *GW*-PRA and *GW*-BSE calculations. It is expected that the tunable optical spectra and E_b could have great potential for their optoelectronic device applications.

Finally, it is also interesting to investigate the order-disorder phase transition temperatures T_c for these five ordered $(BN)_{1-x}(C_2)_x$ ground states on Cr(0001), which can provide a general guideline for the synthesis of disordered $(BN)_{1-x}(C_2)_x$ at the entire x range. Interestingly, the highest T_c for these ordered configurations is found to be ∼1200 K (see Figs. S15–S19 in the Supplemental Material for the MC simulations [38]), as shown in Fig. 5(a). Therefore, it is reasonable to expect that the highest T_c of $(BN)_{1-x}(C_2)_x$ on Cr(0001) in the entire x is also ∼1200 K, as the ground-state configuration at an arbitrary x is always a linear combination of its neighboring two ordered ground-state ones. Considering the experimental temperature (<1000 K) on growing $(BN)_{1-x}(C_2)_x$ [19–24], the homogenous $(BN)_{1-x}(C_2)_x$ could be successfully achieved in the entire x range, which is a great improvement compared to all the previous efforts in the past decade [19–31]. In order to estimate the E_g of disordered $(BN)_{1-x}(C_2)_x$ as a function of x in their free-standing forms, six large-supercell special quasirandom structures (SQS) are selected (see Fig. S20 in the Supplemental Material [14,38,45]). Since it is very challenging to calculate the *GW* band structures of these SQS structures, the HSE06 functional calculations are adopted. As shown in Fig. 5(b), the HSE06-calculated E_g of free-standing disordered $(BN)_{1-x}(C_2)_x$ could be continually tuned from 0 to

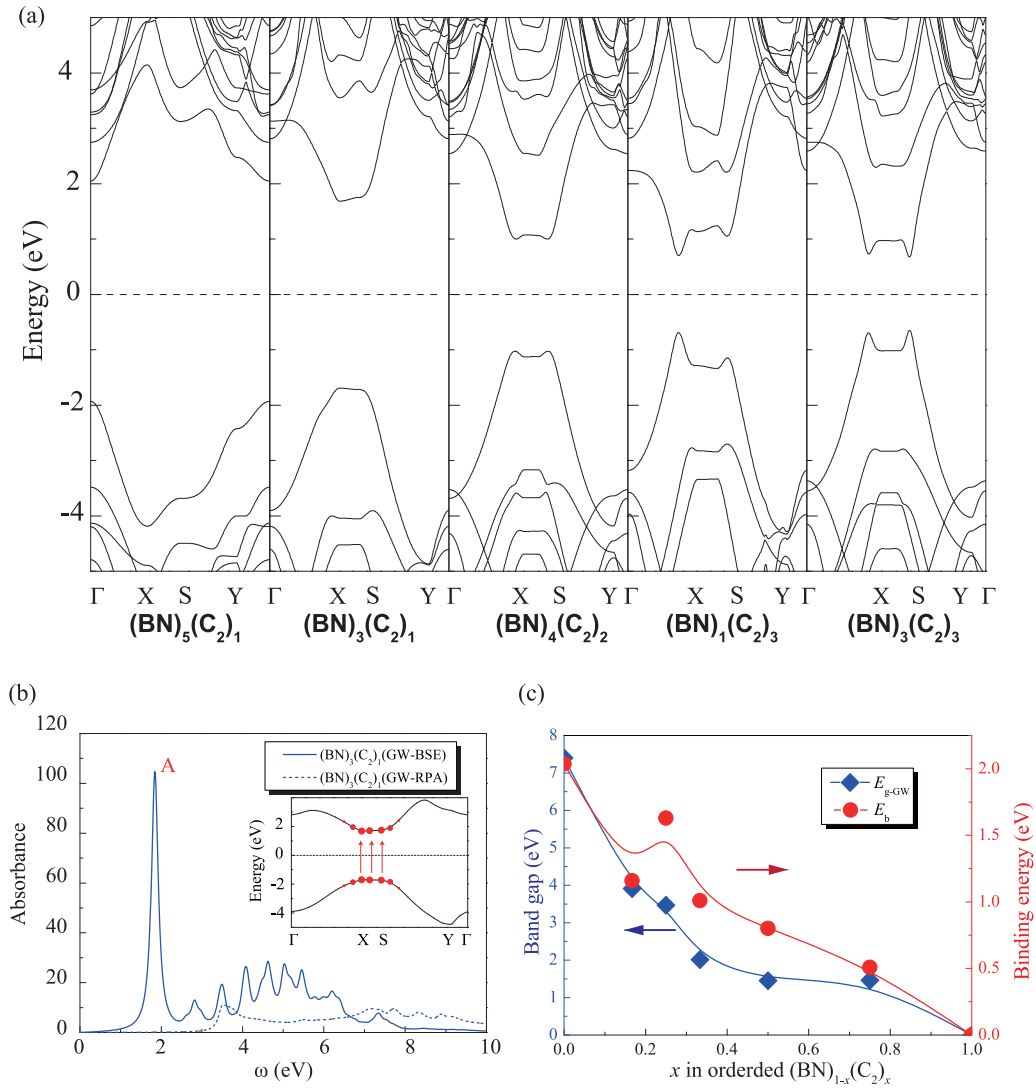

FIG. 4. (a) *GW* band structures of these five ordered $(BN)_{1-x}(C_2)_x$ with different stoichiometries shown in Fig. 2(e). (b) In-plane absorption spectra of $(BN)_3(C_2)_1$ with electron-hole interaction (*GW*-BSE, blue-solid lines) and without electron-hole interaction (*GW*-RPA, blue-dashed lines). Inset shows that the absorption peak (marked as A) at 1.79 eV is contributed by the band-edge optical transitions occurring at these k points associated with flat bands. (c) Calculated *GW* band gap ($E_{g\text{-}GW}$) and exciton binding energies (E_b) of these five ordered $(BN)_{1-x}(C_2)_x$ together with BN and graphene. The E_b is determined by the energy difference of the first absorption peak at the absorption edges between *GW*-PRA and *GW*-BSE calculations.

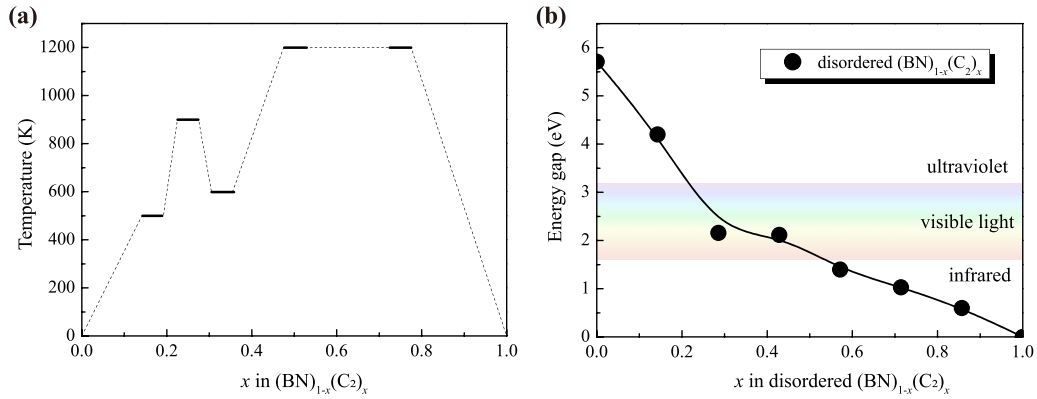

FIG. 5. (a) MC-simulated order-disorder phase transition temperatures for these five intermediate ordered $(BN)_{1-x}(C_2)_x$ alloys grown on Cr(0001). (b) HSE06-calculated band gaps of disordered $(BN)_{1-x}(C_2)_x$ alloys as a function of x.

5.7 eV (see Fig. S21 in the Supplemental Material [38]). Our calculations strongly indicate that $(BN)_{1-x}(C_2)_x$ in their free-standing forms could be the ideal monolithic alloy systems that can cover the entire energy range from infrared to deep-UV spectrums, as long as they can be achieved in their solid solution phases.

III. DISCUSSION

It is noted that the interaction with Cr substrate could make the whole $(BN)_{1-x}(C_2)_x$/Cr system metallic. Therefore, the $(BN)_{1-x}(C_2)_x$ monolayer needs to be peeled off for practice applications. In addition, a new approach, i.e., synthesis-transfer-fabrication process, has recently been developed to realize the device application for monolayer materials with strong substrate interactions, even without the exfoliation process. It has been successfully applied to the silicene/Ag system [46]. It is expected that this approach could also been applied to the $(BN)_{1-x}(C_2)_x$/Cr(0001) system for further device applications.

To conclude, we have proposed an effective concept to greatly enhance the SS in 2D materials, as demonstrated in BNC alloys (one of the most difficult but also the most important cases). This concept, in principle, can be applied to realize various 2D solid solutions with high-energy wrong bonds. Our study could significantly extend our current knowledge on enhancing SS in semiconducting alloys. Once confirmed by the following experiments, the disordered BNC solid solutions, which can cover the entire energy regions from infrared to deep ultraviolet in their free-standing forms, could have great opportunities for many optoelectonic applications from infrared to deep ultraviolet.

IV. METHODS

All the first-principles density functional theory (DFT) calculations are preformed using VASP package with the GGA-PBE for exchange correlation functional [47]. The cut-off energy for plane wave basis is set to be 520 eV. A Γ-centered k-point grid that is generated automatically (2000 k points per reciprocal atom) to make the mesh as uniform in the reciprocal space for different alloy structure. The convergence criterion of electronic step iteration for structural relaxation and a static run after the relaxation is 10^{-5} and 10^{-6} eV, respectively. The vacuum layer is chosen for <12 Å to eliminate the spurious periodic errors along the z direction. A fixed volume relaxation method is applied for freestanding $(BN)_{1-x}(C_2)_x$ structures. For $(BN)_{1-x}(C_2)_x$/TM (TM=Cu, Ni, Cr) structures, the $(BN)_{1-x}(C_2)_x$ alloys are fully optimized on the fixed cleaved three layers TM substrates. The DFT-D3 method is applied to include the van de Waals (vdW) interactions [48]. All the structures are relaxed until the force on each atom is less than 0.01 eV/Å. To accurately estimate the band gaps, the hybrid functional (HSE06) [49] is applied to accurately estimate the electronic structures of disordered $(BN)_{1-x}(C_2)_x$ alloys.

For CE simulation, we have modified the ATAT [35] code in order to effectively calculate the quasibinary $(BN)_{1-x}(C_2)_x$ alloy systems. For the MC simulations, a semi-grand-canonical ensemble is sampled on a superlattice that can contain a sphere with 35 Å radius until the averaging and equilibration time are reached and then phase boundary tracing technique is used to determine the boundary efficiently [36].

For the electronic and optical calculations of ordered $(BN)_{1-x}(C_2)_x$ alloys, the eigenvalues and wave functions obtained from standard first-principles DFT calculations are adopted for GW calculations at one-shot G_0W_0 level. The number of bands (N_b) and energy cutoff ($E_{\text{CUT-}GW}$) in GW calculations are tested carefully to ensure band gaps well converged to <0.05 eV (see Table S2 and Fig. S22 for detailed parameters and convergence test in the Supplemental Material [38]). The Wannier90 code package is used to generate band structures based on the GW calculations [50]. The Bloch functions are projected onto s and p orbitals of B, C, and N, respectively. The energy windows are set about from -5 eV below to $+5$ eV above the Fermi level in which the first-principles calculations are exactly reproduced by the Wannier90 fitting. The Bethe-Salpeter equation (BSE) is solved finally to obtain optical absorption spectra with the consideration of excitonic effects in the basis of previous GW calculations.

For the special quasirandom structures (SQS) simulations, six $(BN)_{1-x}(C_2)_x$ SQSs (98 atoms per supercell) are generated by MC simulations to calculate the electronic structures of fully disordered $(BN)_{1-x}(C_2)_x$ alloys at different x.

ACKNOWLEDGMENTS

We thank Dr. S.-H. Wei at CSRC for the helpful discussions. We acknowledge the support from NSFC (Grants No. 11574024, No. 11674188, and No. 51788104), MOST of China (Grant No. 2016Y-FA0301001), NSAF U1930402, and the Beijing Advanced Innovation Center for Materials Genome Engineering. The calculations were performed at Tianhe2-JK at CSRC.

S.D. and J.W. contributed equally to this work.

[1] A. Gomyo, T. Suzuki, and S. Iijima, Phys. Rev. Lett. **60**, 2645 (1988).
[2] W. Liu, X. Tan, K. Yin, H. Liu, X. Tang, J. Shi, Q. Zhang, and C. Uher, Phys. Rev. Lett. **108**, 166601 (2012).
[3] I. I. Grinberg, D. V. West, M. Torres, G. Gou, D. M. Stein, L. Wu, G. Chen, E. M. Gallo, A. R. Akbashev, P. K. Davies, J. E. Spanier, and A. M. Rappe, Nature (London) **503**, 509 (2013).
[4] H. Ohno, Science **281**, 951 (1998).
[5] C. Huang, J. Feng, F. Wu, D. Ahmed, B. Huang, H. Xiang, K. Deng, and E. Kan, J. Am. Chem. Soc. **140**, 11519 (2018).
[6] P. Chen, X. Liu, J. L. Hedrick, Z. Xie, S. Wang, Q. Lin, M. C. Hersam, V. P. Dravid, and C. A. Mirkin, Science **352**, 1565 (2016).
[7] Y. Yao, Z. Huang, P. Xie, S. D. Lacey, R. J. Jacob, H. Xie, F. Chen, A. Nie, T. Pu, M. Rehwoldt, D. Yu, M. R. Zachariah, C. Wang, R. Shahbazian-Yassar, J. Li, and L. Hu, Science **359**, 1489 (2018).
[8] S. B. Zhang and S.-H. Wei, Phys. Rev. Lett. **86**, 1789 (2001).
[9] B. Huang, M. Yoon, B. G. Sumpter, S.-H. Wei, and F. Liu, Phys. Rev. Lett. **115**, 126806 (2015).

[10] X. Li, M. W. Lin, L. Basile, S. M. Hus, A. A. Puretzky, J. Lee, Y. C. Kuo, L. Y. Chang, K. Wang, J. C. Idrobo, A. P. Li, C. H. Chen, C. M. Rouleau, D. B. Geohegan, and K. Xiao, Adv. Mater. **28**, 8240 (2016).

[11] F. Besenbacher, I. Chorkendorff, B. S. Clausen, B. Hammer, A. M. Molenbroek, J. K. Norskov, and I. Stensgaard, Science **279**, 1913 (1998).

[12] J. Greeley and M. Mavrikakis, Nat. Mater. **3**, 810 (2004).

[13] C. Chen, Y. Kang, Z. Huo, Z. Zhu, W. Huang, H. L. Xin, J. D. Snyder, D. Li, J. A. Herron, M. Mavrikakis, M. Chi, K. L. More, Y. Li, N. M. Markovic, G. A. Somorjai, P. Yang, and V. R. Stamenkovic, Science **343**, 1339 (2014)

[14] B. Huang and S.-H. Wei (eds.), *Handbook of Materials Modeling* (Springer Nature, Switzerland, 2018), Chap. 2.

[15] L. Bergman and J. L. McHale (eds.), *Handbook of Luminescent Semiconductor Materials* (Taylor Francis Group, Boca Raton, FL, 2011).

[16] I. Ho and G. B. Stringfellow, Appl. Phys. Lett. **69**, 2701 (1996).

[17] K. Watanabe, T. Taniguchi, and H. Kanda, Nat. Mater. **3**, 404 (2004).

[18] Y. Kubota, K. Watanabe, O. Tsuda, and T. Taniguchi, Science **317**, 932 (2007).

[19] L. Ci, L. Song, C. Jin, D. Jariwala, D. Wu, and Y. Li, Nat. Mater. **9**, 430 (2010).

[20] M. P. Levendorf, C.-J. Kim, L. Brown, P. Y. Huang, R. W. Havener, D. A. Muller, and J. Park, Nature **488**, 627 (2012).

[21] Z. Liu, L. Ma, G. Shi, W. Zhou, Y. Gong, S. Lei, X. Yang, J. Zhang, J. Yu, K. P. Hackenberg, A. Babakhani, J.-C. Idrobo, R. Vajtai, J. Lou, and P. M. Ajayan, Nat. Nanotechnol. **8**, 119 (2013).

[22] L. Liu, J. Park, D. A. Siegel, K. F. McCarty, K. W. Clark, W. Deng, L. Basile, J. C. Idrobo, A.-P. Li, and G. Gu, Science **343**, 163 (2014).

[23] J. Park, J. Lee, L. Liu, K. W. Clark, C. Durand, C. Park, B. G. Sumpter, A. P. Baddorf, A. Mohsin, M. Yoon, G. Gu, and A.-P. Li, Nat. Commun. **5**, 5403 (2014).

[24] T. Gao, X. Song, H. Du, Y. Nie, Y. Chen, Q. Ji, J. Sun, Y. Yang, Y. Zhang, and Z. Liu, Nat. Commun. **6**, 6835 (2015).

[25] P. Sutter, R. Cortes, J. Lahiri, and E. Sutter, Nano Lett. **12**, 4869 (2012).

[26] Y. Gong, G. Shi, Z. Zhang, W. Zhou, J. Jung, W. Gao, L. Ma, Y. Yang, S. Yang, G. You, R. Vajtai, Q. Xu, A. H. MacDonald, B. I. Yakobson, J. Lou, Z. Liu, and P. M. Ajayan, Nat. Commun. **5**, 3193 (2014).

[27] C. Huang, C. Chen, M. Zhang, L. Lin, X. Ye, S. Lin, M. Antonietti, and X. Wang, Nat. Commun. **6**, 7698 (2015).

[28] M. S. C. Mazzoni, R. W. Nunes, S. Azevedo, and H. Chacham, Phys. Rev. B **73**, 073108 (2006).

[29] K. Yuge, Phys. Rev. B **79**, 144109 (2009).

[30] S. Jungthawan, S. Limpijumnong, and J.-L. Kuo, Phys. Rev. B **84**, 235424 (2011).

[31] N. Berseneval, H.-P. Komsa, V. Vierimaa, T. Björkman, Z. Fan, A. Harju, M. Todorovic, A. V. Krasheninnikov and R. M. Nieminen, J. Phys.: Condens. Matter **29**, 415301 (2017).

[32] L. Song, L. Ci, H. Lu, P. B. Sorokin, C. Jin, J. Ni, A. G. Kvashnin, D. G. Kvashnin, J. Lou, B. I. Yakobson, and P. M. Ajayan, Nano Lett. **10**, 3209 (2010).

[33] Z. Liu, L. Song, S. Zhao, J. Huang, L. Ma, J. Zhang, J. Lou, and P. M. Ajayan, Nano Lett. **11**, 2032 (2011).

[34] B. P. Burton, S. Demers and A. van de Walle, J. Appl. Phys. **110**, 023507 (2011).

[35] A. van de Walle, M. Asta and G. Ceder, Calphad **26**, 539 (2002).

[36] A. van de Walle and M. Asta, Model. Simul. Mater. Sc. **10**, 521 (2002).

[37] M. O. Watanabe, S. Itoh, K. Mizushima, and T. Sasaki, J. Appl. Phys. **78**, 2880 (1995)

[38] See Supplemental Material at http://link.aps.org/supplemental/10.1103/PhysRevB.101.054201 for the parameters used in all the calculations; the first principles and CE calculations of $(BN)_{1-x}(C_2)_x$ on Cu(111)/Ni(111); the structures, the phonon spectrum, the molecular dynamic simulations, the band structures calculated by different methods, the in-plane absorption spectrum, and the snapshots of MC-sampled configurations of five ground-state structures at different temperatures of $(BN)_{1-x}(C_2)_x$ alloys on Cr(0001); the ternary CE calculations of $(BN)_{1-x}(C_2)_x$ on Cr(0001); the in-plane stress tensors and the total energies of metastable and ground states $(BN)_3(C_2)_3$ configurations on Cr(0001); the MC-generated six special quasirandom structures (SQS) of $(BN)_{1-x}(C_2)_x$ alloys at different x with corresponding HSE-calculated band structures; and the convergence test for *GW* calculation;

[39] G. Y. Guo and H. H. Wang, Phys. Rev. B **62**, 5136 (2000).

[40] M. Albrecht, M. Maret, J. Kohler, B. Gilles, R. Poinsot, J. L. Hazemann, J. M. Tonnerre, C. Teodorescu, and E. Bucher, Phys. Rev. Lett. **85**, 5344 (2000).

[41] A. van de Walle, Calphad **33(2)**, 266 (2009).

[42] T. Galvani, F. Paleari, H. P. C. Miranda, A. Molina-Sánchez, L. Wirtz, S. Latil, H. Amara, and F. Ducastelle, Phys. Rev. B **94**, 125303 (2016).

[43] Z. Jiang, Z. Liu, Y. Li, and W. Duan, Phys. Rev. Lett. **118**, 266401 (2017).

[44] M. Bernardi, M. Palummo, and J. C. Grossman, Phys. Rev. Lett. **108**, 226805 (2012).

[45] A. Zunger, S.-H. Wei, L. G. Ferreira, and J. E. Bernard, Phys. Rev. Lett. **65**, 353 (1990).

[46] L. Tao, E. Cinquanta, D. Chiappe, C. Grazianetti, M. Fanciulli, M. Dubey, A. Molle, and D. Akinwande, Nat. Nanotechnol. **10**, 227 (2015).

[47] G. Kresse and J. Furthmüller, Comput. Mater. Sci. **6**, 15 (1996).

[48] S. Grimme, J. Comput. Chem. **27**, 1787 (2006).

[49] J. Heyd, G. E. Scuseria, and M. Ernzerhof, J. Chem. Phys. **118**, 8207 (2003).

[50] G. Pizzi, V. Vitale, R. Arita, S. Blugel, F. Freimuth, G. Géranton, M. Gibertini, D. Gresch, C. Johnson, T. Koretsune, J. Ibanez-Azpiroz, H. Lee, J.-M. Lihm, D. Marchand, A. Marrazzo, Y. Mokrousov, J. I. Mustafa, Y. Nohara, Y. Nomura, L. Paulatto, S. Poncé, T. Ponweiser, J. Qiao, F. Thöle, S. S. Tsirkin, M. Wierzbowska, N. Marzari, D. Vanderbilt, I. Souza, A. A. Mostofi, and J. R. Yates, J. Phys. Cond. Matt. **32**, 165902 (2020).